Lattice dynamics in Sn nanoislands and cluster-assembled films

Kelly Houben,[1,*] Sebastien Couet,[2] Maarten Trekels,[2] Enric Menéndez,[2,†] Tobias Peissker,[1] Jin Won Seo,[3] Michael Y. Hu,[4]
Jiyong Y. Zhao,[4] Esen E. Alp,[4] Sam Roelants,[5] Bart Partoens,[5] Milorad V. Milošević,[5] François M. Peeters,[5]
Dimitrios Bessas,[6,‡] Simon A. Brown,[7] André Vantomme,[2] Kristiaan Temst,[2] and Margriet J. Van Bael[1]

[1]*Laboratory of Solid-State Physics and Magnetism, Celestijnenlaan 200 D, B-3001 Leuven, Belgium*
[2]*Instituut voor Kern- en Stralingsfysica, Celestijnenlaan 200 D, B-3001 Leuven, Belgium*
[3]*Department of Materials Engineering, KU Leuven, Kasteelpark Arenberg 44, B-3001 Leuven, Belgium*
[4]*Advanced Photon Source, Argonne National Laboratory, Argonne, Illinois 60439, USA*
[5]*Departement Fysica, Universiteit Antwerpen, Groenenborgerlaan 171, B-2020 Antwerpen, Belgium*
[6]*European Synchrotron Radiation Facility, F-38043 Grenoble, France*
[7]*Department of Physics and Astronomy, University of Canterbury, Private Bag 4800, Christchurch, New Zealand*

To unravel the effects of phonon confinement, the influence of size and morphology on the atomic vibrations is investigated in Sn nanoislands and cluster-assembled films. Nuclear resonant inelastic x-ray scattering is used to probe the phonon densities of states of the Sn nanostructures which show significant broadening of the features compared to bulk phonon behavior. Supported by *ab initio* calculations, the broadening is attributed to phonon scattering and can be described within the damped harmonic oscillator model. Contrary to the expectations based on previous research, the appearance of high-energy modes above the cutoff energy is not observed. From the thermodynamic properties extracted from the phonon densities of states, it was found that grain boundary Sn atoms are bound by weaker forces than bulk Sn atoms.

I. INTRODUCTION

Phonons, described by the phonon density of states, strongly influence many material properties, such as the mean force constant and the vibrational specific heat [1] as well as thermal, electrical, and mechanical processes and superconductivity. Confined systems exhibit drastically different properties from bulk systems, a phenomenon of great interest to both materials science and microelectronics communities. Bulk systems have been widely investigated, while only a limited number of studies on phonons in nanoscale systems are available. The present study contributes to the understanding of how phonon-related properties evolve with reducing dimensions by investigating phonons in nanometer-sized systems.

The phonon density of states (PDOS) of bulk β-Sn spans a limited energy range up to 18.5 meV [2]. Characteristic features of the PDOS are a broad acoustical phonon peak at 5 meV and broad optical phonon peaks at 15 meV and 16.5 meV [2–6]. The PDOS of low-dimensional systems is expected to be modified due to the restriction of phonon propagation [7–11].

Previously, clear differences between the phonon density of states of bulk and that of nanostructures have been observed, with the following as the most commonly observed anomalies in the phonon spectra of nanostructures: an enhancement of low-energy modes, the appearance of high-energy modes above the cutoff energy of the bulk material, and a broadening of the PDOS features [12–26].

For thin films, the broadening of features in the PDOS was attributed to phonon damping [13,19,27,28] and the enhancement of low-energy phonon modes due to the appearance of surface modes [14,19,27]. In general it was found that for thin films the phonon behavior is strongly influenced by the monolayer in contact with the substrate and the monolayer at the surface.

Nanocrystalline structures with a high density of grain boundaries have been studied theoretically [7,9,26,29] and experimentally [8,12,15,16,18,21,23,24] for different materials. In these nanocrystalline structures, an enhancement of low-energy modes and a broadening of different features of the PDOS were observed. Phonon softening in these structures was attributed to grain boundary atoms and the decrease of the phonon lifetime was attributed to phonon scattering at the grain boundaries [7,8,11,12,15,18,21,23,24]. In some nanocrystalline structures an enhancement of high-energy modes above the cutoff energy was observed which was attributed to surface oxides [12,16], grain boundary atoms [9,21], or changes in the interatomic force constants [11,18,26].

Another type of nanostructure that was studied is isolated nanoparticles [7,8,10,17,20,22,25] for which also an enhancement of low- and high-energy phonon modes as well as a broadening of the PDOS features were observed. The enhancement of low-energy phonon modes was attributed to grain boundary atoms [22] and/or surface atoms [7,8,10,20] or to a weakening of the chemical bonds for surface layer atoms [25]. The enhancement of high-energy modes is due to the contribution of surface oxides or matrix atoms [20,25] or changes in the interatomic force constants [10].

Notwithstanding the vast amount of work on Fe nanostructures, phonons remain poorly understood in many other nanomaterials. Due to, e.g., the mechanical softening at the surface, phonon processes play however an important role in nanomaterials. Phonon confinement can affect phenomena

---

*houben.kelly@gmail.com

†Current address: Departament de Física, Facultat de Ciènces, Universitat Autònoma de Barcelona, E-08193 Bellaterra, Spain.

‡Current address: Fundamental Aspects of Materials and Energy, Department of Radiation Science and Technology, Delft University of Technology, Mekelweg 15, 2629 JB Delft, The Netherlands.
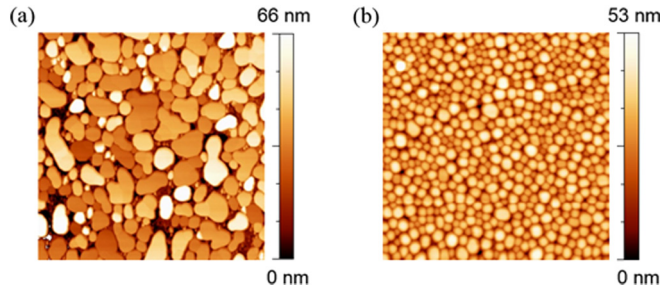
FIG. 1. (a) AFM image (7×7 μm^2) of Sn islands on a clean Si(111) substrate, grown by molecular beam epitaxy; the nominal thickness is 30 nm. (b) AFM image (2×2 μm^2) of a cluster-assembled film resulting from the deposition of Sn clusters on a SiO_2 substrate by a laser-vaporization cluster source; the nominal thickness is 50 nm.

such as thermoelectricity [30–32] or superconductivity [33–35]. Of particular interest are Sn nanostructures because the low sound velocity in Sn (2500 m/s [36]) causes the Van Hove singularities to be located at very low energies. This causes the Sn phonon density of states, as opposed to the PDOS of Fe, to deviate from the Debye behavior already at very low energy. Moreover, Sn is a weak-coupling phonon-mediated superconductor in which phonon softening is expected to result in an enhanced critical temperature. A direct experimental study and clear understanding of the phonon confinement effects of Sn nanostructures is therefore crucial.

In this work, nuclear resonant inelastic x-ray scattering of synchrotron radiation (NRIXS) is used to measure the PDOS in Sn nanostructures. The confinement effects of the lattice dynamics in Sn is studied by analyzing the PDOS of thin nanoscale Sn islands and Sn cluster-assembled films in correlation with the nanoscale morphology of the samples. Flat Sn nanoislands are formed by growing a thin layer of Sn by thermal evaporation in a molecular beam deposition setup on Si(111) substrates, while granular Sn cluster-assembled films are prepared by deposition and aggregation of Sn clusters. Several thermodynamic properties are extracted from the experimentally obtained PDOS, revealing their evolution in the transition from bulk to the nanoscale. The experimental observations are quantified using the damped harmonic oscillation model and highlight the influence of the reduced phonon lifetime and energy broadening due to grain boundary scattering.

II. EXPERIMENTAL DETAILS

Two types of Sn nanostructures with a different morphology have been grown using different deposition techniques, i.e., Sn islands on Si(111) [see Fig. 1(a)] and Sn cluster-assembled films on SiO_2 [see Fig. 1(b)]. The phonon density of states of the different Sn samples was probed by means of the nuclear resonant inelastic x-ray scattering technique (also known as NIS: nuclear inelastic scattering) [37–40]. With this technique, finely monochromatized synchrotron x rays (resolution better than 1 meV) are impinging on the sample. [119]Sn is a Mössbauer active isotope with a nuclear resonance energy of 23.875 keV. When the energy of the incoming x rays equals 23.875 keV, the [119]Sn nuclei go to an excited state;

i.e., the nuclear resonance can be achieved. If the incident photon energy is off-resonance, excitation of the nuclear resonance is achieved via energy exchange with a phonon, i.e., phonon-assisted nuclear resonant absorption. During the decay of the excited nuclei to the ground state, photons are emitted and subsequently detected. The NRIXS spectra are characterized by a peak at zero energy (the energy of the NRIXS spectra is relative to the resonance energy of [119]Sn, i.e., 23.875 keV), which corresponds to the elastic absorption of resonant photons. The side wings of the NRIXS spectrum correspond to phonon-assisted absorption of photons.

NRIXS allows us to probe the full phonon density of states (PDOS) of low-dimensional samples, contrary to Raman spectroscopy which allows us to probe only part of the PDOS while inelastic neutron scattering can only be applied on large-volume samples. Furthermore, the advance in synchrotron instrumentation makes it possible to apply NRIXS to nanoscale Sn samples.

NRIXS measurements on the Sn nanostructures were performed at sector 3-ID of the Advanced Photon Source (Argonne National Laboratory, USA), while NRIXS measurements on a SnO_2 reference powder were performed at the nuclear resonance beamline (ID-18) of the European Synchrotron Radiation Facility (France). Both beamlines are equipped with a high-resolution monochromator with a resolution of 1 meV [3,41]. A grazing incidence scattering geometry was employed and the beam was coarsely focused in the horizontal direction to match the sample size in grazing angle. Measurements were carried out at low temperature (25–35 ± 1 K) using a He-flow cryostat. For the NRIXS measurements, all samples were isotopically enriched (to $97 \pm 1\%$ [119]Sn).

The PHOENIX software [42] was used for the analysis of the NRIXS measurements. Simultaneously with the NRIXS measurements, nuclear forward scattering was detected by a second detector. Nuclear forward scattering proceeds elastically; hence it appears only when the energy of the incident radiation matches exactly the energy of the nuclear resonance. The width of the nuclear transition of [119]Sn is negligible on a scale of keV, so that the data of the second detector provide the instrumental function of the high-resolution monochromator [38]. This instrumental function is matched to the elastic peak of the NRIXS spectra, which is subtracted. The data contain various contributions corresponding to inelastic absorption accompanied by excitation or annihilation of different numbers of phonons. The data are decomposed into n-phonon terms, which enables the derivation of the phonon density of states. The temperature at which the measurements were carried out was confirmed by the detailed balance of phonon creation and annihilation.

Ab initio calculations were done to complement the experimental results. The calculations were performed using the ABINIT [43] DFT package, using a plane-wave basis and working within the local density approximation (LDA), making use of a Trouiller-Martins pseudopotential [44,45] supplied by the Fritz-Haber Institute. The energy associated with the reciprocal wave vectors was chosen to be 1088 eV (i.e., plane-wave cutoff energy) and the Brillouin zone is sampled on a regularly spaced $15 \times 15 \times 15$ grid of k-vectors. The structure is relaxed to its equilibrium lattice spacing at 0 K, which is found to be $a = 0.568$ nm with cell ratio $c/a = 0.541$.

TABLE I. Sn island samples and Sn cluster-assembled films. For the island samples, the thickness refers to the nominal, overall layer thickness (amount of material) aimed for. The thickness values of the cluster samples are obtained from Rutherford backscattering spectrometry.

Sample name	Thickness (nm)	Capping layer
isl60	60	Si (20 nm)
isl40	40	Si (20 nm)
isl20	20	Si (20 nm)
clus18	18	Ge (17 nm)
clus46	46	Ge (17 nm)

This compares well with the room temperature result of $a = 0.583$ nm and $c/a = 0.545$ reported in the literature [46]. The dynamical properties are obtained in an efficient way using density functional perturbation theory (DFPT) to calculate the interatomic force constants, and from there the phonon dynamical matrix elements.

A. Sn islands on Si(111)

Sn islands are formed [Fig. 1(a)] after depositing a thin Sn layer on Si(111) substrates by thermal evaporation in a molecular beam deposition setup at room temperature. The Si substrates were cleaned by a dip in piranha solution (a mixture of H_2SO_4 and H_2O_2 to remove organic residues) for 10 minutes, followed by a 2% HF dip (1 minute) prior to loading them into the vacuum. Isotopically enriched ^{119}Sn was evaporated from a calibrated Knudsen cell under UHV conditions and deposited at room temperature. The evaporation rate of ^{119}Sn was 0.03 Å/s with the Knudsen cell at a temperature of 960 deg C, and the pressure did not exceed 3×10^{-9} mbar during deposition. To prevent oxidation in ambient conditions, one half of each sample was capped at room temperature with a 20 nm Si layer, yielding capped and uncapped parts for comparison. Si was evaporated from a calibrated and ion flux monitored electron beam source.

Table I shows an overview of the different samples with their nominal thickness.

B. Sn cluster-assembled films on SiO$_2$

Sn cluster-assembled films on SiO$_2$ have been prepared in a UHV laser-vaporization setup. A more detailed description of this setup can be found elsewhere [47].

The gas-phase Sn clusters have a size distribution centered at a diameter of about 3.1 nm with a full width at half maximum of 1.1 nm; see Fig. 2(a). The clusters are deposited in a low-energy regime (<1 eV/atom). This ensures a soft landing, thus minimizing cluster deformation and substrate damage. During deposition, the SiO$_2$ substrates were cooled to 200 K using liquid nitrogen. Isotopically enriched ^{119}Sn clusters were deposited onto the SiO$_2$ substrate with a rate of 0.2 Å/s, monitored by a quartz microbalance. When warming up the cluster-assembled film to room temperature, the Sn clusters will transform to the β-Sn phase which is a very fast phase transition. The Sn cluster-assembled film will remain in the β-Sn phase even when cooled down below the phase transition temperature since the β-Sn phase is very stable and
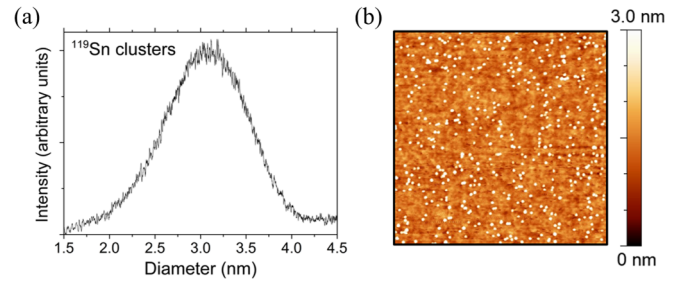
FIG. 2. (a) Size distribution of clusters within the free beam of ^{119}Sn clusters. (b) AFM image (1×1 μm^2) of Sn clusters (white dots) deposited on a SiO$_2$ substrate with a nominal coverage of 0.2 "(cluster) monolayers".

the transition to the α-Sn phase is extremely slow. Figure 2(b) shows an AFM image of Sn clusters deposited on a SiO$_2$ substrate. The Sn clusters are randomly distributed on the substrate, evidencing their low mobility [48]. By continuing cluster deposition up to higher coverages, a Sn cluster-assembled film is created (due to the low-energy deposition and the low mobility of the Sn clusters on a SiO$_2$ substrate). Some degree of coalescence of the Sn clusters is expected [49] in these cluster-assembled films. The base and working pressures in the deposition chamber are 1×10^{-9} mbar and 2×10^{-7} mbar, respectively. The Sn cluster-assembled samples have a thickness of 18 nm and 46 nm (see Table I) and, in order to prevent oxidation, have been capped with a 17 nm thick cluster-assembled Ge film at room temperature. The thickness of the Sn cluster-assembled films was determined by Rutherford backscattering spectrometry (RBS).

To structurally characterize the samples, (grazing incidence) x-ray diffraction [(GI)XRD] was carried out (on a PANalytical X'Pert PRO x-ray diffractometer using Cu K$_{\alpha_1}$ radiation) with an incidence angle of 1 deg. Information on the lattice parameters and typical crystallite sizes of the Sn samples has been extracted from Rietveld refinement of the (GI)XRD patterns [50] using the MAUD software [51]. Information on the composition of the samples has been obtained by conversion electron Mössbauer spectroscopy (CEMS) measurements using the ^{119}Sn Mössbauer isotope. A ^{119m}Sn source in a CaSnO$_3$ matrix is used with a nominal activity of 10 mCi. The Mössbauer spectra were least-squares fitted with the RECOIL program [52] using a Lorentzian line shape. All spectra were recorded at room temperature, and all values of isomer shifts are given with respect to CaSnO$_3$ [53].

A probe-corrected transmission electron microscope (TEM) operating at 200 kV was used to visualize the grain structure of the samples (ARM200F cold-FEG, JEOL). TEM sample preparation involved mechanical and dimple grinding to a thickness of about 10 μm. Finally the sample was thinned to electron transparency by means of ion milling (PIPS, Gatan) using 4 keV and 2 keV.

III. RESULTS AND DISCUSSION

A. Characterization

To obtain information on the topography of the island samples, the uncapped parts of the Sn island samples were
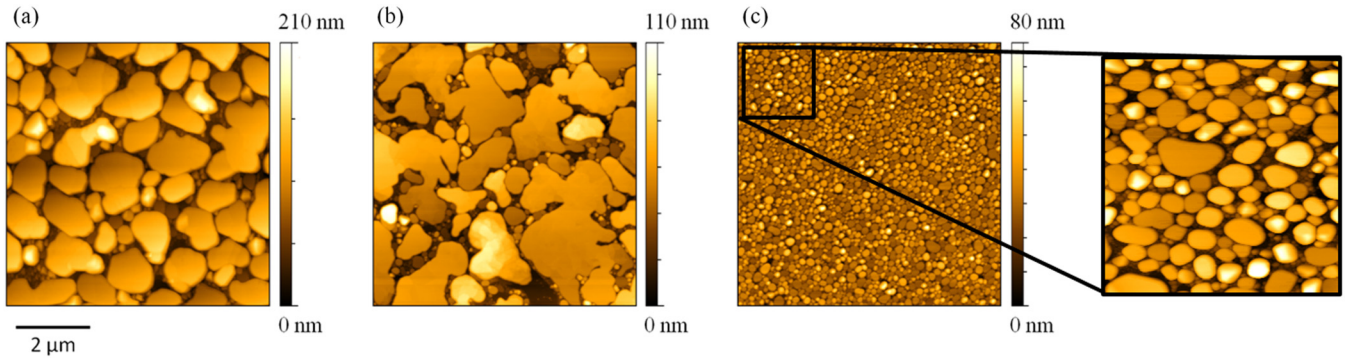
FIG. 3. 7 μm $\times$ 7 μm AFM images of ^{119}Sn islands on Si(111) substrates; nominal thickness of deposited Sn is (a) 60 nm (isl60), (b) 40 nm (isl40), and (c) 20 nm (isl20). A zoom-in (2 μm $\times$ 2 μm) is shown of isl20.

transported (in air) to an atomic force microscope (AFM) [Digital Instruments Dimension system, Nanowizard 3 system (JPK, Germany), and Multimode 8 system (Bruker, USA)]. Figure 3 shows Sn islands corresponding to a nominal deposited thickness of 60 nm (isl60), 40 nm (isl40), and 20 nm (isl20). From the AFM images, it can be seen that Sn forms flat islands on cleaned Si(111) substrates. By varying the nominal thickness, different Sn island size distributions are obtained. From the AFM images, the average island height and surface area per Sn island are obtained (see Table II). The average island height, as well as the rms roughness (overall roughness for a 7 μm $\times$ 7 μm area) increases with increasing nominal thickness. The spread in island height increases with increasing nominal thickness. The total surface coverage remains constant (within the error bar) for all samples. The average surface area per island (average area) is smallest for isl20. For isl40 and isl60 the area of the islands is the same, but the spread in area is larger for isl40. From these findings, it can be concluded that the Sn islands grow laterally and vertically up to a certain island area. After that, only the island height keeps increasing with the amount of deposited Sn.

An AFM image of a typical cluster-assembled film with a thickness of 50 nm is shown in Fig. 1(b). The granular nature of the cluster-assembled films is clearly different from the flat island-like morphology of the Sn islands. From AFM topography images, it is concluded that coalescence of the preformed 3 nm Sn clusters occurred upon deposition. As a result of this coalescence, larger grains are formed, of which the cluster film is composed.

In order to determine the degree of oxidation and the oxidation state of the Sn islands and cluster-assembled films, conversion electron Mössbauer spectroscopy has been used. The CEMS data for all samples correspond to a singlet site for Sn and doublet sites for SnO and SnO$_2$. The singlet site of neutral Sn has an isomer shift (δ) of 2.75 mm/s. The doublet sites for SnO and SnO$_2$ have isomer shifts of 3.9 mm/s and

0.16 mm/s and a quadrupole splitting (Δ) of 1.84 mm/s and 0.38 mm/s, respectively [53].

The composition of the samples has been characterized in detail since the presence of Sn oxide or α-Sn will strongly influence the phonon density of states. In Fig. 4 two CEMS measurements are shown for isl20 with and without a Si capping layer (thickness = 20 nm). Without the capping layer [Fig. 4(a)], a limited oxidation of the Sn islands occurs. The Lamb-Mössbauer factor (f_{LM}) is the fraction of nuclear emission or absorption processes without excitation of phonons in the lattice, indicating that the lower f_{LM}, the lower the corresponding signal in the CEMS measurement will be. Because the Lamb-Mössbauer factor of Sn ($f_{LM} = 0.039$ at room temperature [54]) is much lower than for Sn^{4+} in SnO$_2$ ($f_{LM} = 0.42$ at room temperature [55]) or Sn^{2+} in SnO ($f_{LM} = 0.12$ at room temperature [56]), the amount of Sn in the CEMS measurements is underestimated. By taking into account the Lamb-Mössbauer factor for the different Sn sites, the absolute percentage of the different components is obtained (see Table III). Without the capping layer, the contribution from Sn oxides amounts to 4%. After capping, this fraction decreases to 1% [in Fig. 4(b), the peaks corresponding to SnO$_2$ and SnO have almost completely vanished]. Also for the cluster-assembled films, the SnO$_2$ and SnO contribution is very low (4%), which indicates a negligible oxidation for all samples, with or without the capping layer. None of the samples shows any traces of the α-Sn phase.

Figure 5 shows θ-2θ XRD and GIXRD measurements for samples isl20, isl40, and isl60, while the GIXRD data for clus18 and clus46 samples and rocking curves are shown in Fig. 6. GIXRD measurements are shown in Fig. 5(b) for the island samples and in Fig. 6(a) for the cluster-assembled films. Several reflections of β-Sn are identified which indicates that the Sn islands are not fully epitaxial on the Si(111) substrate. For the cluster-assembled films a polycrystalline nature is revealed; i.e., the films consist of randomly oriented grains.

TABLE II. Information extracted from AFM images of Sn islands on Si(111) substrates.

Sample	Average height (nm)	rms roughness (nm)	Average area (μm^2)	Surface coverage (%)
isl60	100 $\pm$ 21	36 $\pm$ 2	0.6 $\pm$ 0.1	60 $\pm$ 5
isl40	68 $\pm$ 17	23 $\pm$ 1	0.6 $\pm$ 0.2	71 $\pm$ 5
isl20	50 $\pm$ 11	17 $\pm$ 1	0.016 $\pm$ 0.001	68 $\pm$ 5

FIG. 4. (a) CEMS measurements of 20 nm Sn islands without Si capping layer (isl20). (b) 20 nm Sn islands with Si capping layer (isl20 C).

TABLE III. Absolute percentages of the different Sn sites for different nominal thicknesses of Sn islands on Si(111) substrates with (C) and without Si capping layer, as well as for the Sn cluster-assembled films [all capped with a Ge capping layer (C)].

Sample	Sn^{4+}	β-Sn	Sn^{2+}
isl60	2 ± 2	98 ± 2	0
isl40	1 ± 2	99 ± 2	0
isl20	3 ± 2	96 ± 2	1 ± 2
isl20 C	1 ± 2	99 ± 2	0
clus18 C	1 ± 2	99 ± 2	0
clus46 C	2 ± 2	98 ± 2	0

films was estimated via Rietveld refinement of the GIXRD measurements. The results are shown in Table IV. A typical crystallite size of the order of 60 nm can be found in all samples, with a somewhat smaller value ($\propto 40$ nm) for sample clus18. It should be noted that these are averaged values and that each sample contains a variety of crystallite sizes and shapes (see also below).

By using a standard θ-2θ geometry, the rocking curves [see Fig. 6(b)] of the island samples and cluster films have been measured. A large difference in the width of the curves corresponding to isl60 and clus46 is observed [see Fig. 6(b)]. The same is true for the other island samples and cluster-assembled film. The rocking curve of the island samples indicates a low mosaicity (a small spread of crystal orientations) while the cluster films exhibit a high mosaicity (a large spread of crystal orientations).

In general it is concluded from the XRD measurements that the cluster-assembled Sn films are polycrystalline. The Sn islands are textured: the islands consist of crystallites with a preferred orientation according to the Si substrate.

When using NRIXS, the measured PDOS is the PDOS projected on the wave vector of the incident photon. However, due to the limited texture of the Sn islands samples, this effect can be neglected in this work.

Figure 7 shows a TEM image of sample isl40C. The configuration of flat islands (dark areas) of different sizes is very comparable to the AFM image in Fig. 3(b). In the TEM image, it can be clearly seen that each island consists of many crystallites and that the larger as well as the smaller islands contain a lot of internal grain boundaries (see different gray

The θ-2θ XRD measurements of the Sn islands [Fig. 5(a)] and the cluster-assembled films [Fig. 5(c)] reveal that the Sn islands are more textured than the cluster-assembled films.

The typical crystallite size (average coherently diffracting domain size) of the Sn islands and the cluster-assembled
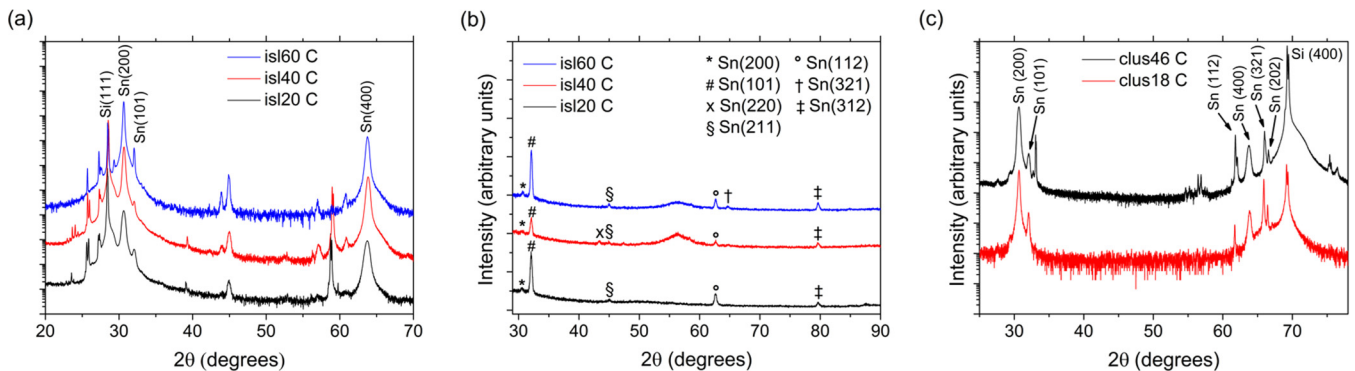
FIG. 5. (a) θ-2θ XRD measurements. (b) GIXRD measurements at a grazing incidence angle of 1 deg for the different island samples, aligned according to the substrate. (c) θ-2θ XRD measurements for the two cluster-assembled films.

(a)

(b)
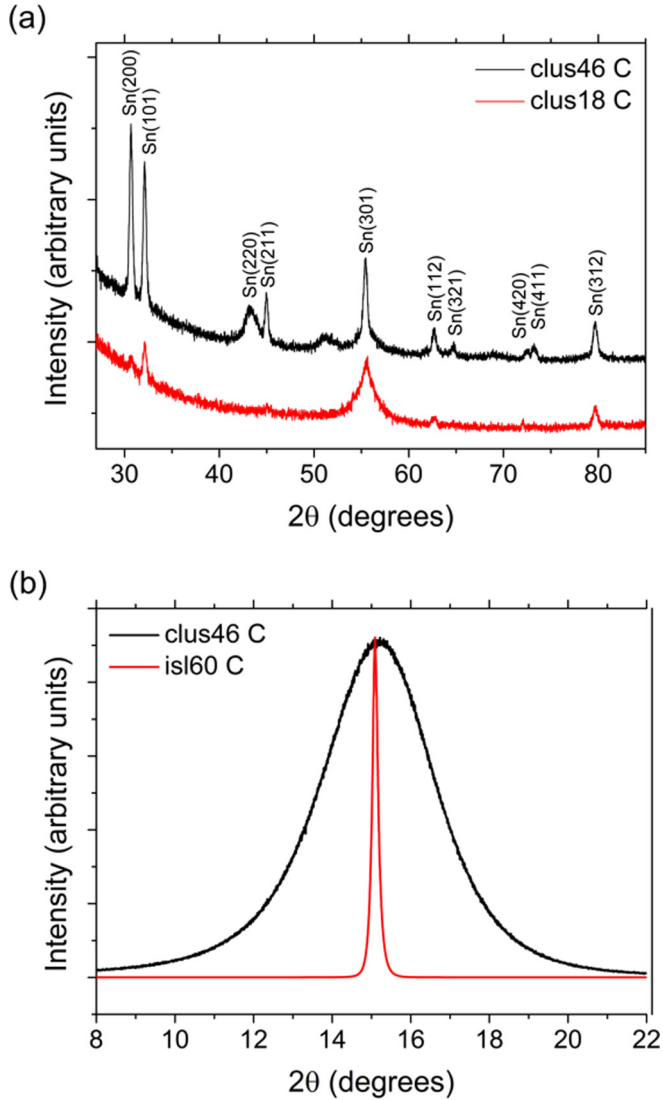
FIG. 6. (a) GIXRD measurements, with an incidence angle of 1 deg, of the cluster-assembled films. (b) Rocking curves of the Sn(200) peak for isl60 C and clus46 C (detector position $2\theta = 30.676$ deg).

contrast within one grain). It is also clear that crystallites have a large size range and very different shapes within a single sample. Note that for this TEM image, the sample was tilted to obtain high contrast for the grains, especially in the larger

TABLE IV. Crystallite size for the different Sn nanostructures obtained from Rietveld refinement of GIXRD measurements and the quality factor (Q) obtained from the damped harmonic oscillator (DHO) model. Note that for the island samples, this crystallite size implies that each island contains several crystallites.

Sample	Crystallite size (nm)	Q factor (DHO)
isl60 C	63 ± 8	18 ± 2
isl40 C	53 ± 9	17 ± 2
isl20 C	65 ± 3	14 ± 3
clus18 C	35 ± 9	22 ± 3
clus46 C	64 ± 4	12 ± 2
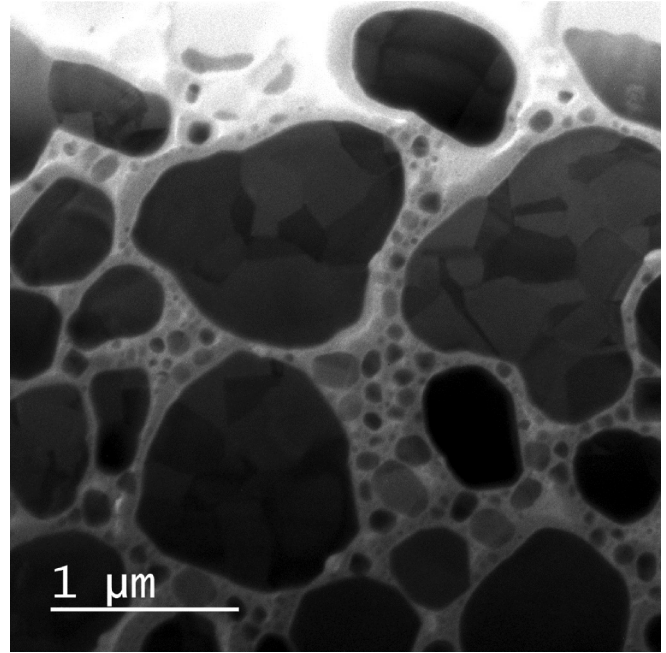
FIG. 7. Planar view bright-field TEM image of sample is l40C. All islands (dark contrast) consist of grains with different crystalline orientations, which can be seen as sections with different gray contrast within one grain.

islands. This image condition was not ideal for many other grains, especially those in the smaller islands. This implies that not all grain orientations and grain boundaries are visible in this image.

B. Phonon density of states

In Fig. 8(a), the phonon densities of states of a reference ^{119}Sn foil (thickness $= 0.35$ mm) and SnO$_2$ powder are shown. The energy range of the PDOS of the metallic Sn foil extends up to 18.5 meV, in agreement with the cutoff energy of bulk β-Sn, while the range of the PDOS of SnO$_2$ powder is much broader and the cutoff energy is 40 meV. The experimentally obtained PDOSs of the reference β-Sn foil and the nanostructured samples are compared to *ab initio* calculations of the lattice dynamics properties of bulk β-Sn. The resulting calculated PDOS is shown in Fig. 8(b) (full curve) and is compared to the experimentally obtained PDOS of the reference ^{119}Sn foil. As can be seen from the figure, the features of the experimentally obtained PDOS are very well reproduced by the calculation, in particular the peaks at 5 meV and 15 meV and the dip at 9.5 meV, characteristic of the PDOS of bulk β-Sn. The calculated PDOS is in very good agreement with bulk Sn PDOS calculations found in literature [57,58]. Furthermore, the calculated dispersion curves of bulk β-Sn capture very well the behavior of bulk β-Sn dispersion curves obtained by inelastic neutron scattering experiments [59].

The measured PDOSs for the Sn island and cluster-assembled samples are shown in Figs. 9(a) and 9(b), respectively. No contribution of SnO$_2$ to the phonon spectra of the island and cluster samples (which would show up at energies between 20 and 45 meV) is observed, in agreement with the CEMS results. When comparing the phonon spectra of the
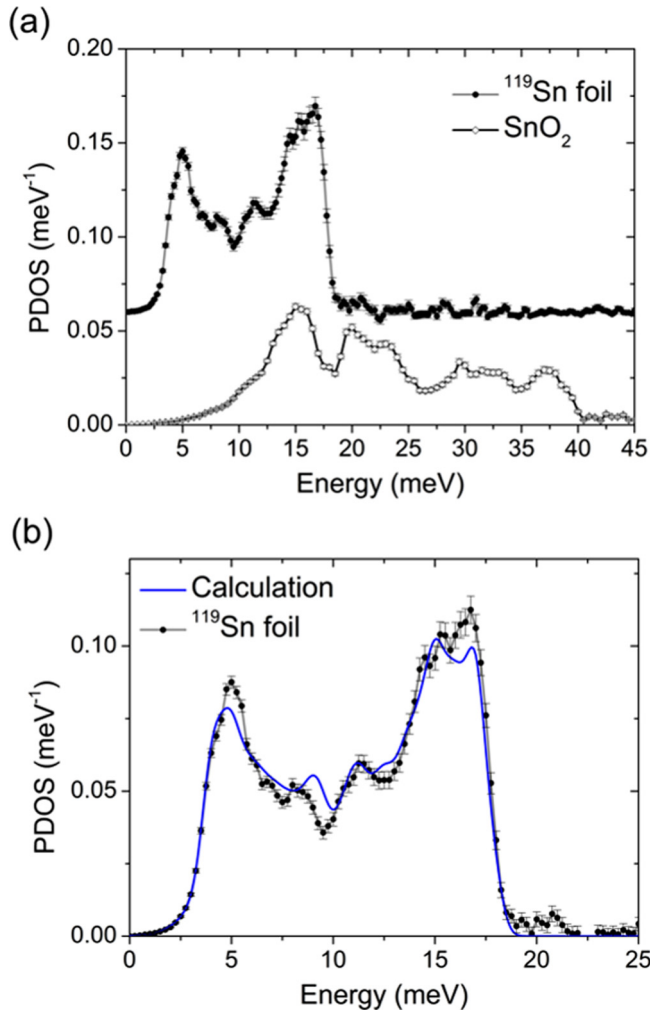
FIG. 8. (a) PDOS of a ^{119}Sn foil (vertically shifted by 0.06 meV^{-1} for clarity) and a SnO$_2$ powder, for reference purposes. (b) Comparison of calculated PDOS (solid line) with the experimentally obtained PDOS of a ^{119}Sn foil.

Sn nanostructures with bulk Sn (Fig. 9), four features can be observed: (i) a decrease of high-energy modes; (ii) an increase of low-energy modes, see Fig. 10; (iii) an increase of intermediate phonon modes; and (iv) a broadening of the
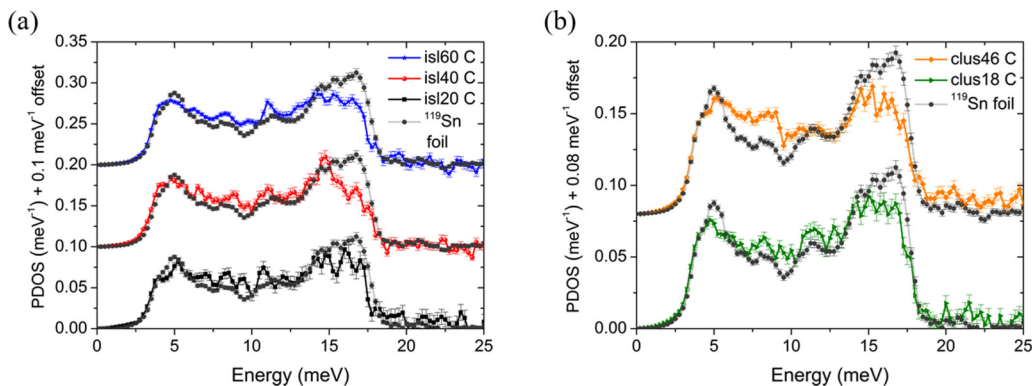
PDOS features. We will now discuss these four observations in more detail.

(i) The decrease in intensity of high-energy modes (15 and 18 meV) was observed before in various nanoscale systems [12,13,16,19,21–25], an effect which was found to originate from phonon scattering. From the TEM study, it was concluded that a single Sn island is composed of many Sn crystallites. The grain boundaries in between these crystallites can cause an increased phonon scattering rate. Also for the Sn cluster-assembled films, a high density of grain boundaries is present within the cluster films. However, the decrease of high-energy modes is usually accompanied by the appearance of energy modes above the cutoff energy [9,13,20,21,25,26], which is not observed here.

(ii) The slight enhancement of low-energy modes between 1 and 4 meV (see Fig. 10; also known as phonon softening) is similar to what was observed before in small Sn nanoparticles (diameter ∝ 11 nm) embedded in a porous glass matrix [25], where a substantial fraction of Sn atoms was located at the surface, giving rise to phonon softening. For the nanostructured samples which are studied here, one can expect a substantial fraction of Sn atoms residing at or close to grain boundaries, also resulting in a slight increase of low-energy phonon modes. This indicates that for a fraction of Sn atoms, the interatomic interaction is weaker than for bulk Sn.

As mentioned in the Introduction, contrary to Fe, there is a limited validity of the Debye law for Sn (the Debye law is valid from 0 up to ≈3 meV), which does not allow a reliable investigation of the Debye behavior in Sn nanostructures.

The appearance of high-energy modes above the cutoff energy is usually attributed to the influence of the matrix or the capping layer on surface Sn atoms [25]. In this work, the grain boundary Sn atoms are only in contact with other Sn atoms, although in a position of reduced symmetry. The presence of oxygen atoms is excluded considering the CEMS results. The absence of oxides might explain the absence of high-energy modes above the cutoff energy.

(iii) The enhancement of intermediate phonon modes (6.5–13 meV) is a consequence of the decreased high-energy phonon modes leading to a redistribution of modes.

In Fig. 11, the PDOS of isl60 with and without Si capping layer is shown. The Si capping layer does not have a pronounced effect on the phonon density of states or on the

FIG. 9. (a) PDOS measured at $25 - 35 \pm 1$ K for the different Sn island samples. (b) PDOS measured at $25 - 35 \pm 1$ K for Sn cluster-assembled films of 18 nm and 46 nm nominal thickness.

(a)

(b)
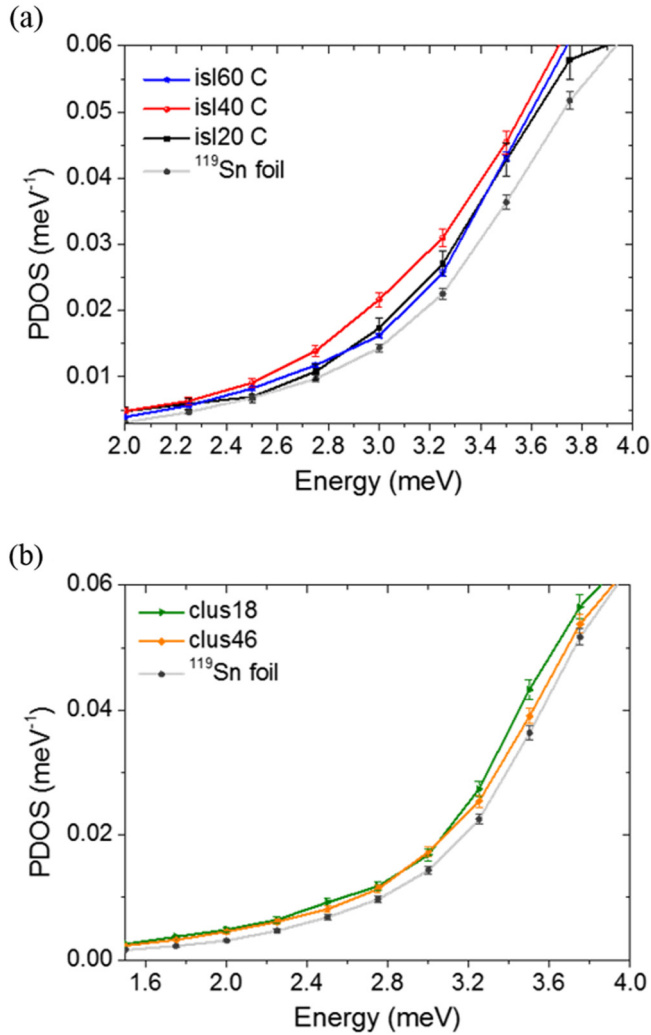
FIG. 10. (a) Low-energy range of the PDOS of the different Sn island samples. (b) Low-energy range of the PDOS of Sn cluster-assembled films.

thermodynamic properties. From the CEMS measurements, it is known that there is no significant difference in the amount of oxidation with or without Si capping. In both cases, the amount of oxidation is too small to have a significant influence on the phonon spectrum [such as the appearance of high-energy (>20 meV) SnO_2 phonon modes].

The Sn island samples and the Sn cluster-assembled films show very similar features in their PDOSs, which are dominated by the high density of grain boundaries.

(iv) In order to elucidate the effects of phonon scattering on the phonon density of states and to explain the broadened features in the PDOS, the damped harmonic oscillator (DHO) model was applied to all measured PDOSs.

C. Damped harmonic oscillator model

One of the main assumptions of *ab initio* phonon calculations is the use of a harmonic approximation which implies an infinite phonon lifetime, while in a real system the phonon lifetime is reduced because of scattering due to the presence of grain boundaries, impurities, interactions between phonons,
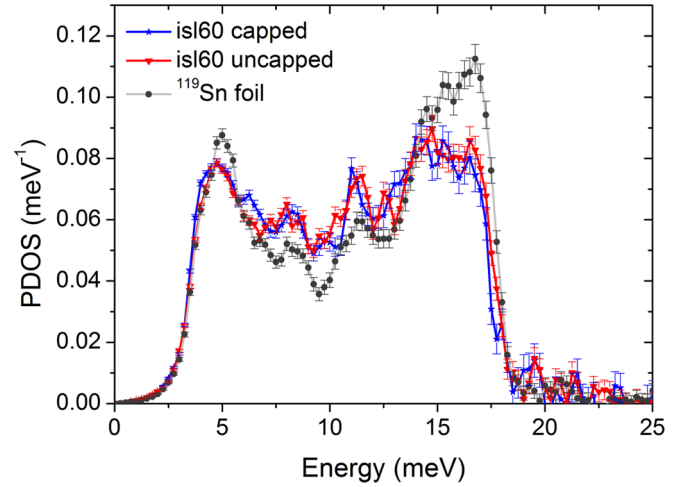
FIG. 11. Phonon density of states isl60 with and without Si capping layer.

etc. Reduced phonon lifetimes are expected in bulk systems, but even more so in granular or confined geometries. This reduced phonon lifetime causes an energy broadening of phonon lines resulting in a broadening of all features of the PDOS. It can be described within the damped harmonic oscillator (DHO) model [60,61], which incorporates the line broadening, as a function of energy E, as follows:

$$D(E', E) = \frac{1}{\pi Q E'} \frac{1}{(E'/E - E/E')^2 + 1/Q^2}. \quad (1)$$

$D(E', E)$ is a damped harmonic oscillator function which is convoluted with the theoretical PDOS. The only free parameter is Q, the quality factor of the oscillator. When Q is large, $D(E', E)$ resembles a Lorentzian function centered at E' with a FWHM of approximately E'/Q. The lower the Q value, the shorter the lifetime of the phonon state, and the broader the features in the phonon spectrum. For simplicity, Q is assumed to have the same average value for all phonon modes in our analysis, which has proven to be a successful method to describe phonon lifetime broadening in metallic nanostructures [13,19,60]. The aim of using the DHO model here is to provide a simple model to explain the overall changes observed in the experimental phonon spectra. The DHO model only incorporates phonon damping (broadening of the phonon modes), whereas a redistribution of phonon modes, new phonon modes, shifts of the cutoff energy, etc., are not taken into account.

The DHO model was applied to the calculated PDOS for bulk Sn and compared to the experimentally obtained phonon spectrum of the Sn foil. The best agreement with the experimental PDOS is obtained for a high Q value of $Q = 80 \pm 6$. This long phonon lifetime confirms the bulk behavior of the Sn foil. The DHO model has also been applied to the PDOS measured for the various Sn nanostructures; see Fig. 12. In Table IV, the obtained Q values are shown. The different Sn nanostructures reveal Q values that are considerably lower than that of the Sn foil, indicating strong phonon damping. For all Sn island samples as well as for

(a)

(b)
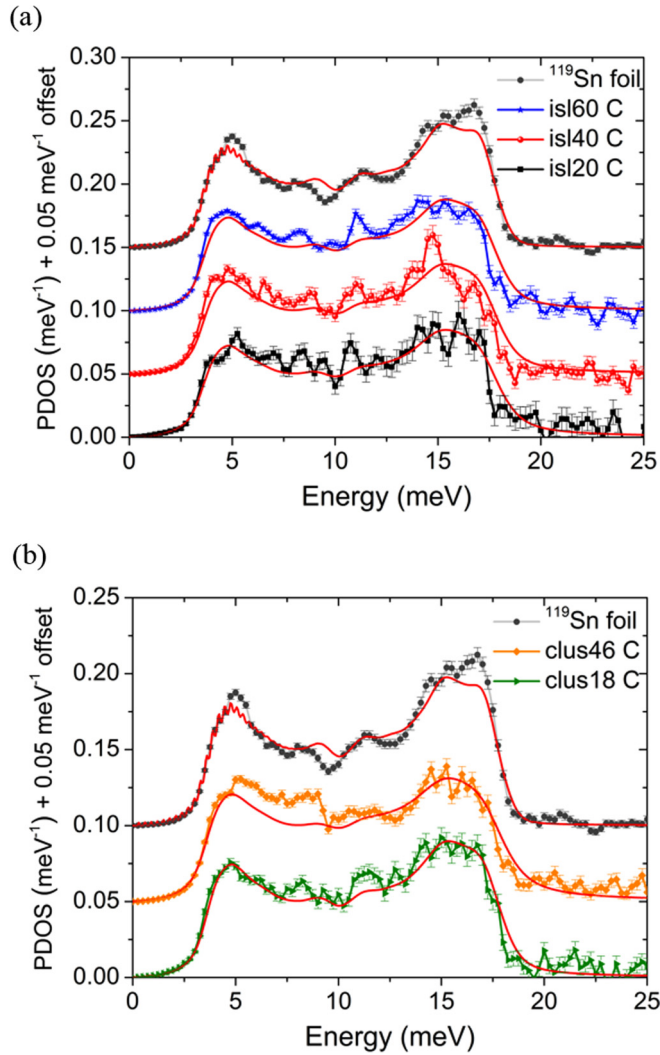
FIG. 12. (a) PDOS of the different Sn island samples. (b) PDOS of the cluster-assembled films. In both figures, the red solid curves are the fits obtained by applying the DHO model.

sample clus18, a similar Q factor of the order of 15–20 is obtained, while the Q factor for sample clus46 is lower.

For a simple DHO, the relation between Q and the lifetime is given by $t = 2Q/w$ with w the vibration frequency. A Q factor of the order of 20, as we have in our nanoscale samples, corresponds to a lifetime of the order of 16 ps, where $w = 2.4 \times 10^{12}$ Hz = 10 meV is used as the typical phonon frequency. In order to test the plausibility that grain boundary scattering is at the origin of this energy broadening and reduced lifetime, a simple order of magnitude estimation can be made to see whether we find a similar lifetime of a few 10 ps when considering grain boundary scattering. Assuming purely diffusive scattering, the phonon lifetime is estimated as $t = v/D = 20$–24 ps with v the phonon velocity in Sn (2500 m/s for bulk Sn) and D the typical size of a grain (our samples have typical crystallite sizes of 50–60 nm).

This good correspondence can be seen as a confirmation that grain boundary scattering is one of the main reasons for the shortened lifetime and resulting energy broadening. Not all features observed in the PDOSs of the Sn nanostructures

TABLE V. Thermodynamic properties of atomic dynamics at 35 K calculated from the experimentally obtained PDOS of the different Sn island samples and cluster-assembled films. f_{LM} denotes the Lamb-Mössbauer factor, B the mean force constant, $\langle u^2 \rangle$ the mean-squared atomic displacement, S the vibrational entropy, and C the vibrational specific heat.

Sample	f_{LM}	B (N/m)	$\langle u^2 \rangle$ (pm^2)	S (k_B)	C (k_B)
isl60 C	0.65 ± 0.02	61 ± 6	29 ± 2	0.75 ± 0.02	1.30 ± 0.05
isl40 C	0.65 ± 0.03	61 ± 6	29 ± 3	0.74 ± 0.04	1.29 ± 0.08
isl20 C	0.66 ± 0.05	67 ± 11	28 ± 6	0.69 ± 0.06	1.22 ± 0.12
clus18 C	0.66 ± 0.02	65 ± 6	29 ± 2	0.71 ± 0.04	1.24 ± 0.08
clus46 C	0.66 ± 0.02	63 ± 5	28 ± 2	0.72 ± 0.03	1.27 ± 0.06
bulk foil	0.67 ± 0.02	69 ± 3	27 ± 2	0.67 ± 0.02	1.19 ± 0.05

are explained by the DHO model, such as the slightly enhanced low-energy part (1–4 meV) of the PDOSs of all Sn nanostructured samples. Evidently, this enhancement does not originate from phonon damping. However, in general, a very good agreement between the DHO model and the experimental PDOS is obtained, even despite the assumption of the same Q for all phonons. This implies that the features in the vibrational behavior of nanoislands and cluster films are dominated by a reduced phonon lifetime caused predominantly by phonon scattering at grain boundaries.

D. From vibrational dynamics to thermodynamics

Various thermodynamic quantities, e.g., mean force constant and specific heat, depend intimately on the system's phonon density of states. Due to the changes in the phonon behavior at the nanoscale, it is expected that these thermodynamic quantities experience a corresponding evolution. The densities of phonon states (shown in Fig. 9) up to 20 meV were used to calculate [38,42,62] several thermodynamic parameters characterizing the atomic dynamics [38] in the Sn island samples and Sn cluster-assembled films. This allows us to probe the influence of the changes in the phonon behavior on the thermodynamic quantities. The range of the densities of phonon states was limited to 20 meV to avoid taking into account the noise at higher energies (20–25 meV) for the calculation of the thermodynamic properties. The results are shown in Table V. The deduced Lamb-Mössbauer factor f_{LM}, the mean force constant B, and the mean-squared atomic displacement $\langle u^2 \rangle$ for the bulk Sn foil agree very well with values that were found in earlier work for bulk Sn ($f_{LM} = 0.69 \pm 0.01$, $B = 74 \pm 1$ N/m, and $\langle u^2 \rangle = 25 \pm 1$ pm^2 found in Ref. [25]).

In general, it is observed that the values for B of the nanostructures are lower than for bulk, while the values for $\langle u^2 \rangle$, S, and the vibrational specific heat (C) are higher. This can be attributed to the high density of grain boundaries in each nanostructured Sn sample. The Sn atoms in these grain boundaries experience a reduced symmetry and coordination compared to bulk Sn atoms. As a consequence these Sn atoms are held in place by weaker forces than bulk Sn atoms which locally increases the atomic displacement [63], hence also the vibrational entropy. One can consider f_{LM} as a measure for the stiffness of the lattice. The tendency of a slight decrease in

f_{LM} is hence in perfect agreement with the slight decrease of the mean force constant in comparison to bulk Sn. For different nanoscale materials [7,22,26] the specific heat was observed to be larger than the corresponding bulk value, as is the case here: an increase of the specific heat of 3–11% in comparison to bulk Sn was found.

IV. CONCLUSIONS

In this work, the phonon density of states was investigated by NRIXS for two different types of Sn nanostructures: flat Sn nanoislands and granular Sn cluster-assembled films which have in common that they consist of many nanoscale crystallites (of the order of 40–60 nm) separated by grain boundaries. The structure, morphology, and purity of the different samples was characterized by combining (GI)XRD, AFM, TEM, RBS, and CEMS. The experimentally obtained phonon spectra have been successfully reproduced by applying the damped harmonic oscillator model to the calculated bulk PDOS for β-Sn. The PDOSs of Sn nanostructures with a different morphology can be described within the same model with one single parameter, i.e., the quality factor Q. This indicates that the changes in the vibrational behavior are dominated by phonon lifetime broadening, in particular phonon scattering at grain boundaries.

Aside from a broadening of the features in the phonon spectra, a decrease in intensity of high-energy phonon modes and a slight enhancement of low-energy phonon modes (phonon softening) was observed. These observations are explained by the high density of grain boundaries in all nanostructured samples studied in this work. Contrary to what was observed for different nanocrystalline materials, no high-energy phonon modes above the cutoff energy were observed for the islands and the cluster films.

Several thermodynamic properties were extracted from the measured PDOSs of the different types of Sn nanostructures. It was found that the Sn atoms in the grain boundaries are bound by weaker forces than bulk Sn atoms, which results in a larger atomic displacement and hence an increase in the vibrational entropy.

Our experiments have been conducted using state-of-the-art monochromator technologies. However, in view of the low-energy dynamics of Sn, even more interesting information could eventually be obtained with better energy resolution in the μeV regime, e.g., to detect possible deviations from the Debye behavior. While this is currently not possible, developments are ongoing for improving the energy resolution towards the 100 μeV range [64,65].

A future challenge is to correlate the changes in the phonon density of states at the nanoscale to changes in the superconducting behavior. β-Sn is a low-temperature superconductor with a bulk superconducting transition temperature (T_C) of 3.7 K. A substantial increase in (T_C) of Sn nanostructures has been experimentally observed [33,66,67] with origins in the subtle interplay of the quantum confinement for the electronic degrees of freedom and a phonon environment [68]. Our work enables further analysis of the role of phonon confinement in nanoscale superconductivity, and its precise account in Sn nanostructures.

[1] D. Bozyigit, N. Yazdani, M. Yarema, O. Yarema, W. M. M. Lin, S. Volk, K. Vuttivorakulchai, M. Luisier, F. Juranyi, and V. Wood, Nature (London) **531**, 618 (2016).

[2] A. I. Chumakov, A. Barla, R. Rüffer, J. Metge, H. F. Grünsteudel, H. Grünsteudel, J. Plessel, H. Winkelmann, and M. M. Abd-Elmeguid, Phys. Rev. B **58**, 254 (1998).

[3] A. Barla, R. Rüffer, A. I. Chumakov, J. Metge, J. Plessel, and M. M. Abd-Elmeguid, Phys. Rev. B **61**, R14881 (2000).

[4] D. L. Price, Proc. R. Soc. London, Ser. A **300**, 25 (1967).

[5] A. S. Ivanov, N. L. Mitrofanov, and A. Y. Rumiantsev, Physica B (Amsterdam, Neth.) **213**, 423 (1995).

[6] J. M. Rowe, Phys. Rev. **163**, 547 (1967).

[7] R. Meyer, L. J. Lewis, S. Prakash, and P. Entel, Phys. Rev. B **68**, 104303 (2003).

[8] D. Şopu, J. Kotakoski, and K. Albe, Phys. Rev. B **83**, 245416 (2011).

[9] P. M. Derlet and H. V. Swygenhoven, Phys. Rev. Lett. **92**, 035505 (2004).

[10] A. Kara and T. S. Rahman, Surf. Sci. Rep. **56**, 159 (2005).

[11] D. Y. Sun, X. G. Gong, and X. Q. Wang, Phys. Rev. B **63**, 193412 (2001).

[12] B. Fultz, C. C. Ahn, E. E. Alp, W. Sturhahn, and T. S. Toellner, Phys. Rev. Lett. **79**, 937 (1997).

[13] R. Röhlsberger, W. Sturhahn, T. S. Toellner, K. W. Quast, P. Hession, M. Y. Hu, J. Sutter, and E. E. Alp, J. Appl. Phys. **86**, 584 (1999).

[14] T. Ślęzak, J. Łażewski, S. Stankov, K. Parlinski, R. Reitinger, M. Rennhofer, R. Rüffer, B. Sepiol, M. Ślęzak, N. Spiridis, M. Zajac, A. I. Chumakov, and J. Korecki, Phys. Rev. Lett. **99**, 066103 (2007).

[15] E. Bonetti, L. Pasquini, E. Sampaolesi, A. Deriu, and G. Cicognani, J. Appl. Phys. **88**, 4571 (2000).

[16] L. Pasquini, A. Barla, A. I. Chumakov, O. Leupold, R. Rüffer, A. Deriu, and E. Bonetti, Phys. Rev. B **66**, 073410 (2002).

[17] Y. Tsunoda, Y. Kurimoto, M. Seto, S. Kitao, and Y. Yoda, Phys. Rev. B **66**, 214304 (2002).

[18] A. F. Yue, A. B. Papandrew, O. Delaire, B. Fultz, Z. Chowdhuri, R. M. Dimeo, and D. A. Neumann, Phys. Rev. Lett. **93**, 205501 (2004).

[19] S. Stankov, R. Röhlsberger, T. Ślęzak, M. Sladecek, B. Sepiol, G. Vogl, A. I. Chumakov, R. Rüffer, N. Spiridis, J. Łażewski, K. Parliński, and J. Korecki, Phys. Rev. Lett. **99**, 185501 (2007).

[20] B. Roldan Cuenya, A. Naitabdi, J. Croy, W. Sturhahn, J. Y. Zhao, E. E. Alp, R. Meyer, D. Sudfeld, E. Schuster, and W. Keune, Phys. Rev. B **76**, 195422 (2007).

[21] S. Stankov, Y. Z. Yue, M. Miglierini, B. Sepiol, I. Sergueev, A. I. Chumakov, L. Hu, P. Svec, and R. Rüffer, Phys. Rev. Lett. **100**, 235503 (2008).

[22] B. Roldan Cuenya, L. K. Ono, J. R. Croy, K. Paredis, A. Kara, H. Heinrich, J. Zhao, E. E. Alp, A. T. DelaRiva, A. Datye *et al.*, Phys. Rev. B **86**, 165406 (2012).

[23] H. Frase, B. Fultz, and J. L. Robertson, Phys. Rev. B **57**, 898 (1998).

[24] U. Stuhr, H. Wipf, K. H. Andersen, and H. Hahn, Phys. Rev. Lett. **81**, 1449 (1998).

[25] P. P. Parshin, M. G. Zemlyanov, G. K. Panova, A. A. Shikov, Y. A. Kumzerov, A. A. Naberezhnov, I. Sergueev, W. Crichton, A. I. Chumakov, and R. Rüffer, J. Exp. Theor. Phys. **114**, 440 (2012).

[26] R. Singh and S. Prakash, Surf. Sci. **532**, 272 (2003).

[27] J. Łażewski, J. Korecki, and K. Parlinski, Phys. Rev. B **75**, 054303 (2007).

[28] S. Couet, H. Peelaers, M. Trekels, K. Houben, C. Petermann, M. Y. Hu, J. Y. Zhao, W. Bi, E. E. Alp, E. Menéndez, B. Partoens, F. M. Peeters, M. J. Van Bael, A. Vantomme, and K. Temst, Phys. Rev. B **88**, 045437 (2013).

[29] P. M. Derlet, R. Meyer, L. J. Lewis, U. Stuhr, and H. Van Swygenhoven, Phys. Rev. Lett. **87**, 205501 (2001).

[30] P. Kim, L. Shi, A. Majumdar, and P. L. McEuen, Phys. Rev. Lett. **87**, 215502 (2001).

[31] B. Poudel, Q. Hao, Y. Ma, Y. Lan, A. Minnich, B. Yu, X. Yan, D. Wang, A. Muto, D. Vashaee *et al.*, Science **320**, 634 (2008).

[32] D. G. Cahill, W. K. Ford, K. E. Goodson, G. D. Mahan, A. Majumdar, H. J. Maris, R. Merlin, and S. R. Phillpot, J. Appl. Phys. **93**, 793 (2003).

[33] B. Abeles, R. W. Cohen, and G. Cullen, Phys. Rev. Lett. **17**, 632 (1966).

[34] K. Knorr and N. Barth, Solid State Commun. **8**, 1085 (1970).

[35] P. B. Allen, Solid State Commun. **14**, 937 (1974).

[36] G. V. Samsonov, *Handbook of the Physicochemical Properties of the Elements* (IFI-Plenum, New York, 1968).

[37] R. Röhlsberger, *Nuclear Condensed Matter Physics with Synchrotron Radiation: Basic Principles, Methodology and Applications* (Springer, Berlin, 2004).

[38] A. I. Chumakov and W. Sturhahn, Hyperfine Interact. **123**, 781 (1999).

[39] W. Sturhahn, T. S. Toellner, E. E. Alp, X. Zhang, M. Ando, Y. Yoda, S. Kikuta, M. Seto, C. W. Kimball, and B. Dabrowski, Phys. Rev. Lett. **74**, 3832 (1995).

[40] D. Bessas, W. Töllner, Z. Aabdin, N. Peranio, I. Sergueev, H. Wille, O. Eibl, K. Nielsch, and R. P. Hermann, Nanoscale **5**, 10629 (2013).

[41] T. S. Toellner, M. Y. Hu, G. Bortel, W. Sturhahn, and D. Shu, Nucl. Instrum. Methods Phys. Res., Sect. A **557**, 670 (2006).

[42] W. Sturhahn, Hyperfine Interact. **125**, 149 (2000).

[43] X. Gonze, B. Amadon, P. M. Anglade, J. M. Beuken, F. Bottin, P. Boulanger, F. Bruneval, D. Caliste, R. Caracas, M. Côté, T. Deutsch, L. Genovese, P. Ghosez, M. Giantomassi, S. Goedecker, D. R. Hamann, P. Hermet, F. Jollet, G. Jomard, S. Leroux, M. Mancini, S. Mazevet, M. J. T. Oliveira, G. Onida, Y. Pouillon, T. Rangel, G. M. Rignanese, D. Sangalli, R. Shaltaf, M. Torrent, M. J. Verstraete, G. Zerah, and J. W. Zwanziger, Comput. Phys. Commun. **180**, 2582 (2009).

[44] N. Troullier and J. L. Martins, Phys. Rev. B **43**, 1993 (1991).

[45] M. Fuchs and M. Scheffler, Comput. Phys. Commun. **119**, 67 (1999).

[46] N. W. Ashcroft and D. Mermin, *Solid State Physics* (Saunders, Philadelphia, 1976).

[47] N. Vandamme, E. Janssens, F. Vanhoutte, P. Lievens, and C. Van Haesendonck, J. Phys.: Condens. Matter **15**, S2983 (2003).

[48] V. N. Popok, Mater. Sci. Eng., R **72**, 137 (2011).

[49] A. Perez, P. Melinon, V. Dupuis, P. Jensen, B. Prevel, J. Tuaillon, L. Bardotti, C. Martet, M. Treilleux, M. Broyer, M. Pellarin, J. L. Vaille, B. Palpant, and J. Lerme, J. Phys. D: Appl. Phys. **30**, 709 (1997).

[50] R. A. Young, Cryst. Res. Technol. **30**, 494 (1995).

[51] L. Lutterotti, S. Matthies, and H. R. Wenk, IUCr: Newsletter of the CPD, No. **21**, 14 1999.

[52] D. G. Rancourt and J. Y. Ping, Nucl. Instrum. Methods Phys. Res., Sect. B **58**, 85 (1991).

[53] J. G. Stevens, Hyperfine Interact. **13**, 221 (1983).

[54] C. Hohenemser, Phys. Rev. **139**, A185 (1965).

[55] M. T. Sougrati, S. Jouen, and B. Hannoyer, Hyperfine Interact. **167**, 815 (2006).

[56] M. S. Moreno and R. C. Mercader, Phys. Rev. B **50**, 9875 (1994).

[57] S. Na and C. Park, J. Korean Phys. Soc. **56**, 494 (2010).

[58] P. Pavone, S. Baroni, and S. de Gironcoli, Phys. Rev. B **57**, 10421 (1998).

[59] *Phonon States of Elements, Electron States, and Fermi Surfaces of Alloys*, edited by H. R. Schober, P. H. Dederichs, D. J. Sellmyer, K. H. Hellwege, and J. L. Olsen, Landolt-Börnstein, New Series, Group III, Vol. 13, Pt. A (Springer, Berlin, 1981).

[60] B. Fultz, Prog. Mater. Sci. **55**, 247 (2010).

[61] B. Fåk and B. Dorner, Application of the damped harmonic oscillator model to lattice vibrations, Institut Laue Langevin Technical Report No 92FA008S, Institut Laue Langevin, 1992 (unpublished).

[62] M. Y. Hu, T. S. Toellner, N. Dauphas, E. E. Alp, and J. Zhao, Phys. Rev. B **87**, 064301 (2013).

[63] J. W. Garland, K. H. Bennemann, and F. M. Mueller, Phys. Rev. Lett. **21**, 1315 (1968).

[64] T. S. Toellner, M. Y. Hu, W. Sturhahn, G. Bortel, E. E. Alp, and J. Zhao, J. Synchrotron Radiat. **8**, 1082 (2001).

[65] Y. Shvyd'ko, S. Stoupin, K. Mundboth, and J. Kim, Phys. Rev. A **87**, 043835 (2013).

[66] M. Strongin, O. F. Kammerer, J. E. Crow, R. D. Parks, D. H. Douglass Jr., and M. A. Jensen, Phys. Rev. Lett. **21**, 1320 (1968).

[67] S. Bose, A. M. García-García, M. M. Ugeda, J. D. Urbina, C. H. Michaelis, I. Brihuega, and K. Kern, Nat. Mater. **9**, 550 (2010).

[68] M. D. Croitoru, A. A. Shanenko, A. Vagov, M. V. Milošević, V. M. Axt, and F. M. Peeters, Sci. Rep. **5**, 16515 (2015).